Downwelling-Front Instability and Eddy Formation in the Eastern Mediterranean

YIZHAK FELIKS* AND MICHAEL GHIL**

Climate Dynamics Center and Department of Atmospheric Sciences, University of California, Los Angeles, California

(Manuscript received 11 July 1991, in final form 7 February 1992)

ABSTRACT

The instability of the downwelling front along the southern coast of Asia Minor is studied with a multimode quasigeostrophic model. Linear analysis shows that the most unstable wave has a length of about 100 km. The wavelength depends only very weakly on the transversal scale of the front. The wave period is larger by an order of magnitude than the e-folding time; that is, rapid local growth occurs with little propagation. The growth rate is proportional to the maximum of the speed of the downwelling westward jet.

The evolution of the frontal waves can be divided into three stages. At first, the evolution is mainly due to linear instability; the second stage is characterized by closed eddy formation; and finally, isolated eddies separate from the front and penetrate into the open sea. The largest amount of available potential energy is transferred to kinetic energy and into the barotropic mode during the second, eddy-forming stage, when several dipoles develop in this mode. The formation of anticyclonic eddies is due to advection of the ridges of the unstable wave's first baroclinic mode by the barotropic dipole. The baroclinic eddies ride on the barotropic dipoles. The propagation of such dipole-rider systems is determined mainly by the evolution of the corresponding barotropic dipole.

These results suggest that the warm- and salty-core eddies observed in the Eastern Mediterranean are due, at least in part, to the instability of the downwelling front along the basin's northeastern coastline. There is both qualitative and quantitative similarity between the observed and calculated eddies in their radius (35–50 km), thermal structure, and distribution along the coast.

1. Introduction

Eddies with warm and salty cores have been shown to exist in the Eastern Mediterranean by Feliks and Itzikowitz (1987), Hecht et al. (1988), and Ozsoy et al. (1989). In these eddies the 14°–16°C isotherms slope downward by 100–300 m over a horizontal distance of about 50 km. The same slope was observed in the 38.75–39.05 psu isohalines. The water type in the core of these eddies, down to 450 m, is that of Levantine Intermediate Water (LIW) in its region of formation by downwelling along the Asia Minor coast. Some eddies were observed down to depths of 800–900 m, and could persist in the region for more than a year.

Feliks (1990) studied numerically the evolution of an isolated vortex in a four-mode β-plane ocean model and showed that such a vortex can persist for several simulated years. He proposed that a barotropic modon with a baroclinic rider, which develops in this model, is a good idealization for Eastern Mediterranean warm-core eddies. The validity of this modon–rider system as a persistent eddy model is due to its being nondispersive for a long period of time and its speed of propagation being mainly determined by the mean current advection.

Feliks (1991) studied further, in a multilayer Boussinesq system with rotation, the downwelling along the northeastern coasts of the Eastern Mediterranean induced by winter storms, the so-called Cyprus cyclones. He showed that intensive downwelling and a westward current develop along the south coast of Asia Minor in an alongshore band about 100 km wide. The temperature and salinity profiles in the downwelling zone are very similar to those observed in the Mediterranean eddies with warm and salty cores.

Feliks suggested that baroclinic instability may act in the downwelling front to create significant meandering and that later, due to nonlinear dynamics, eddies will detach from the front. Baroclinic instability mechanisms had been proposed for the California Current system by Mysak (1977), Hukuda (1982), and Ikeda (1983) to explain the meandering of the upwelling front. Their studies were able to explain some of the observed features, like the wavelength and growth rate, based on the length of the most unstable wave of the corresponding linear model.

---

* On sabbatical leave from the Department of Mathematics, Israel Institute for Biological Research.

** Also affiliated with the Institute of Geophysics and Planetary Physics, University of California, Los Angeles, California.

Corresponding author address: Prof. Michael Ghil, Department of Atmospheric Sciences, University of California, Los Angeles, CA 90024-1565.

A different mechanism for coastal-front instabilities, somewhat related to Kelvin–Helmholtz instability, was proposed by Paldor and Ghil (1991), with some encouraging comparisons to the meandering of the Algerian Current in the Western Mediterranean. Ghil and Paldor (1991) showed that the initial, weakly nonlinear evolution of frontal instabilities on a coupled density front is dominated by the linearly most unstable waves.

In this paper we study the instability of the downwelling front, along with eddy formation and detachment, using a quasigeostrophic numerical model with four vertical modes. In section 2 the mathematical formulation of the problem is presented. In section 3 the linear instability is studied in terms of normal modes in the vertical, rather than levels. In section 4 the development and detachment of eddies is described. In section 5 the dependence of the results on several parameters is examined. Concluding remarks follow in section 6.

2. Mathematical model

In this study we use a quasigeostrophic rigid-lid model with several modes in the vertical, following Feliks (1990). The model equations are nondimensionalized by the following characteristic scales:

$$X, Y \propto L, \quad Z \propto H, \quad t \propto \frac{L}{V} = T, \quad \psi \propto VL,$$

where V is the particle speed, L is the Rossby radius of deformation of the first baroclinic mode, and H is the vertical scale. The appropriate scales for the Eastern Mediterranean downwelling case are listed in Table 1.

The nondimensional potential vorticity equation with this scaling is

$$\frac{\partial q}{\partial t} + \beta \frac{\partial \psi}{\partial x} + J(\psi, q) = 0, \tag{2.1a}$$

where

$$q = \nabla^2 \psi + \frac{\partial}{\partial z}\left(\frac{1}{S}\frac{\partial \psi}{\partial z}\right), \tag{2.1b}$$

$$S = \frac{N^2 H^2}{f^2 L^2}, \quad \beta = \beta_0 \frac{L^2}{V}, \tag{2.1c,d}$$

f is the value of the Coriolis parameter at a central latitude (34°N), $N(z)$ is the mean Brunt–Väisälä frequency, and β_0 is the meridional gradient of f at the central latitude. The mean Brunt–Väisälä frequency in the following numerical experiments (Fig. 1a) was taken from the end of the downwelling simulation described by Feliks (1991).

The vertical structure of the model is based on the eigenfunctions $\phi_k(z)$ of the eigenvalue problem

$$\frac{\partial}{\partial z}\left(\frac{1}{S}\frac{\partial \phi_k}{\partial z}\right) = -\lambda_k^2 \phi_k, \tag{2.2}$$

with the boundary condition $\partial\phi_k/\partial z = 0$ at the sea surface $z = 0$ and at the mean depth $z = -H_0$. We designate by $k = 0$ the barotropic mode, and by $k = 1, 2, \cdots$ the successive baroclinic modes. The external Rossby radius of deformation, L/λ_0, is infinite, according to the rigid-lid assumption; the kth internal Rossby radius of deformation is L/λ_k, $k = 1, 2, \cdots$. The first three internal radii are listed in Table 1, and the first four eigenfunctions, one barotropic and three baroclinic, are shown in Fig. 1b.

We decompose the streamfunction ψ and the potential vorticity q into vertical normal modes:

$$\psi(x, y, z, t) = \sum_k \psi_k(x, y, t)\phi_k(z), \tag{2.3a}$$

$$q(x, y, z, t) = \sum_k q_k(x, y, t)\phi_k(z). \tag{2.3b}$$

The equations for the modal amplitudes (Flierl 1978) are

$$\frac{\partial q_k}{\partial t} + \beta \frac{\partial \psi_k}{\partial x} + \sum_{i,j} \xi_{ijk} J(\psi_i, q_j) = 0, \quad 0 \leqslant k \leqslant 3, \tag{2.4a}$$

where

$$q_k = \nabla^2 \psi_k - \lambda_k^2 \psi_k, \quad \xi_{ijk} = \frac{1}{H_0}\int_{-H_0}^{0} \phi_i \phi_j \phi_k dz; \tag{2.4b,c}$$

ξ_{ijk} are the triple interaction coefficients, and their values for the downwelling case are given in Table 1.

TABLE 1. The scales and the physical parameters for the downwelling.

V (cm s^{-1})	L (km)	H (m)	T (days)	β_0 (cm^{-1} s^{-1})	$\beta = \beta_0 \frac{L^2}{V}$
5	10	2000	2.31	1.82×10^{-13}	0.364

mode k	L/λ_k (km)
1	9.4
2	3.8
3	2.4

ijk	$\xi_{ijk} = \frac{1}{H_0}\int_{-H_0}^{0} \phi_i\phi_j\phi_k dz$
000	1.00
011	1.00
022	1.00
033	1.00
111	2.60
112	0.75
113	0.24
122	0.56
123	0.72
222	−1.31
223	−0.39
233	−0.98
333	−0.81

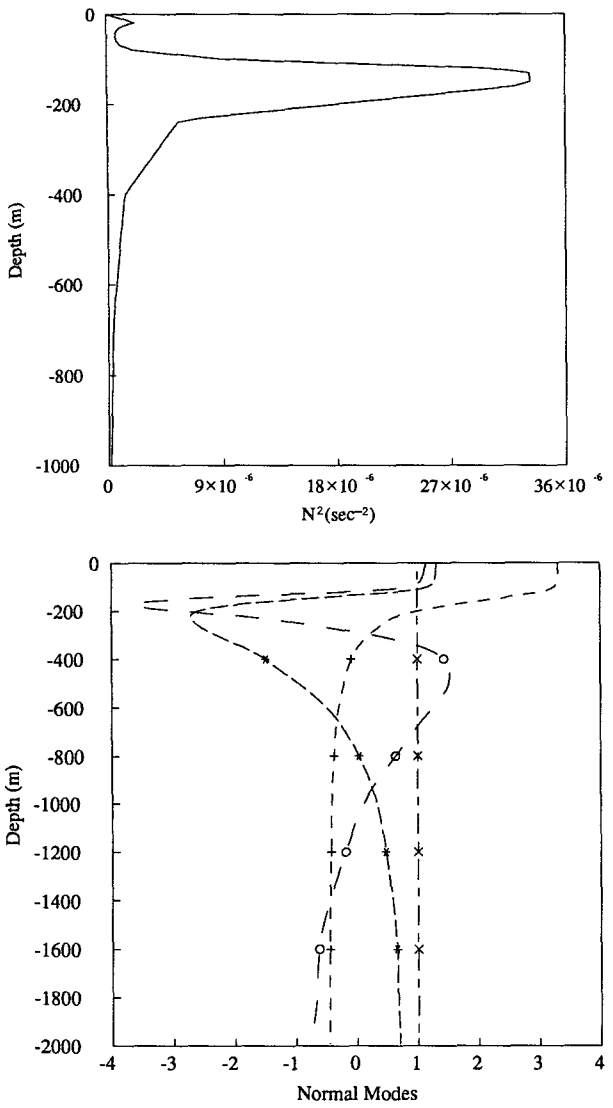

FIG. 1. (a) The vertical profile of N^2 in the downwelling simulation of Feliks (1991). (b) The first four vertical modes: the barotropic one (× with long-short dashes) and the first three baroclinic modes.

The integration domain is rectangular of size 1458 km × 576 km. This domain has a coast along its northern boundary ($y = 0$, Fig. 4a). The basic state is a coastal jet flowing westward along the northern boundary of the form

$$\bar{\psi}(x, y, z) = ae^{-y^2/b^2}\phi_1(z), \tag{2.5a}$$

$$\bar{q}(x, y, z) = ae^{-y^2/b^2}\left\{\frac{2}{b^2}\left(\frac{2y^2}{b^2} - 1\right) - \lambda_1^2\right\}\phi_1(z). \tag{2.5b}$$

This jet describes fairly well the downwelling front and the baroclinic part of the coastal jet obtained in the simulation of Feliks (1991). The values of the intensity parameter a and the width parameter b are determined by the maximum speed of the jet, u_0, and the distance from the coast of this maximum, y_0, respectively:

$$a = u_0 y_0 e^{1/2}/VL, \quad b = y_0\sqrt{2}/L. \tag{2.6a,b}$$

The appropriate values for the Anatolian downwelling case are $y_0 = 50$ km and $u_0 = 6$ cm s^{-1}.

Feliks (1991) showed that the width of the jet is proportional to the square root of the horizontal diffusion coefficient. Due to uncertainty in the value of that coefficient, the location of the maximum of the jet is also uncertain. Hence, we examine the stability of different jets as a function of y_0 in section 5c.

The streamfunction on the boundaries is time independent. Along the coast $v \equiv \partial\psi/\partial x = 0$; that is, ψ is constant along the coast. To calculate the potential vorticity on the coast we assume nonslip conditions; that is, $u \equiv -\partial\phi/\partial y = 0$.

The numerical scheme is the same as in Feliks (1990). Key features include fourth-order accurate discretization by finite elements in the horizontal (cf. Haidvogel et al. 1980), a second-order Adams–Bashforth scheme in time, and a fourth-order Shapiro (1970) filter for every time step. A uniform grid of 244 × 97 points in the horizontal was used, with a spatial and temporal resolution of $\Delta x = \Delta y = 6$ km$/L$ and $\Delta t = 2700$ s$/T$, except in sections 3b and 5c, where a higher resolution was introduced for comparison purposes.

The fourth-order filter has a very similar effect to viscous dissipation. It can be shown that the filter is equivalent to adding the following higher-order diffusion term to the right-hand side of Eq. (2.4a),

$$A\nabla^4 q_k = A\nabla^4(\nabla^2\psi_k - \lambda_k^2\psi_k), \tag{2.7}$$

where $A = (1/16)\Delta x^4 \Delta t$. For the resolution given above and used in most of the experiments, $A = 0.6$ in nondimensional units, or $A = 3 \times 10^{18}$ cm^4 s^{-1}.

3. Linear instability

a. *Linearization and eigenproblem*

Many linear instability studies of coastal and ocean currents are based on layer models (e.g., Mysak 1977; Haidvogel and Holland 1978; Ikeda 1983; Paldor and Ghil 1991). In the following we study the stability of the downwelling jet with a model based on vertical normal modes rather than on layers.

Linearizing Eq. (2.4) about the downwelling jet (2.5), we superimpose on this jet a perturbation that has the form of a wave propagating along the coast; that is,

$$\psi'(x, y, z, t) = \sum_j e^{ik(x-ct)} D_j(y)\phi_j(z), \tag{3.1}$$

where $\psi' = 0$ at $y = 0$ and $y \to -\infty$. Here c is the wave

speed and k the wavenumber. The perturbation for each vertical mode j has the form:

$$\psi_j' = e^{ik(x-ct)}D_j(y), \tag{3.2a}$$

$$q_j' = [-(k^2 + \lambda_j^2)D_j + d^2D_j/dy^2]e^{ik(x-ct)}. \tag{3.2b}$$

After some mathematical manipulations, we get the following set of second-order ordinary differential equations for the vertical modes of the perturbation:

$$c[D_j'' - (k^2 + \lambda_j^2)D_j] = \beta D_j + \sum_l D_l\xi_{jl2} \times [\bar{q}' + \bar{\psi}'(k^2 + \lambda_l^2)] - \sum_l D_l''\xi_{jl2}\bar{\psi}', \tag{3.3}$$

where $\bar{\psi}$ and $\bar{q}$ are defined in (2.5), and ξ_{jl2} by (2.4c). The boundary conditions are $D_j = 0$ at $y = 0$, $y \to -\infty$. The eigenvalue c and the eigenfunctions D_j are functions of $\bar{\psi}$ and k. All the other parameters are determined by the mean stratification $N(z)$.

The solution of the eigensystem (3.3) is obtained numerically as follows. The second derivative with respect to y is approximated by second-order differences,

$$\frac{d^2D_j}{dy^2} \approx \frac{D_j(y + \Delta y) + D_j(y - \Delta y) - 2D_j(y)}{\Delta y^2}, \tag{3.4}$$

so Eqs. (3.3) become

$$c\left[\frac{D_j(y + \Delta y)}{dy^2} + \frac{D_j(y - \Delta y)}{dy^2} - D_j(y)(k^2 + \lambda_j^2 + 2/\Delta y^2)\right] = \beta D_j(y) + \sum_m \frac{D_m(y + \Delta y)}{\Delta y^2}\xi_{jm2}\frac{2y}{b^2}ae^{-y^2/b^2} + \sum_m \frac{D_m(y - \Delta y)}{\Delta y^2}\xi_{jm2}\frac{2y}{\Delta y^2}ae^{-y^2/b^2} + \sum_m D_m(y)\xi_{jm2}\frac{2y}{b^2}ae^{-y^2/b^2} \times \left(\frac{-2}{\Delta y^2} - \frac{4y^2}{b^4} + \frac{6}{b^2} + \lambda_2^2 - \lambda_m^2 - k^2\right). \tag{3.5}$$

This homogeneous linear system can be written in vector–matrix notation as

$$c\mathbf{Ad} = \mathbf{Bd}; \tag{3.6}$$

$\mathbf{d}$ is the matrix having as its columns the discretized eigenfunctions

$$\mathbf{d} = (\mathbf{d}_1^T, \mathbf{d}_2^T, \cdots, \mathbf{d}_n^T)^T, \tag{3.7a}$$

where $(\ )^T$ is the transpose, n is the number of vertical modes, and

$$\mathbf{d}_j = (D(y_1), \cdots, D(y_l))^T, \quad 1 \leq j \leq n, \tag{3.7b}$$

with l the number of grid points in the y direction.

The matrix $\mathbf{A}$ is block diagonal:

$$\mathbf{A} = \text{diag}(\mathbf{A}_j), \tag{3.8a}$$

where each $\mathbf{A}_j$ is an $(l \times l)$ tridiagonal symmetric matrix; the elements on the main diagonal are equal to $-(k^2 + \lambda_j^2 + 2/\Delta y^2)$, and the elements on the upper and lower subdiagonals are both equal to $1/\Delta y^2$,

$$-\mathbf{A}_j = \text{tridiag}(-1/\Delta y^2, k^2 + \lambda_j^2 + 2/\Delta y^2, -1/\Delta y^2). \tag{3.8b}$$

The matrix $\mathbf{B}$ has the form

$$\mathbf{B} = \begin{pmatrix} \mathbf{B}_1^1 & \mathbf{B}_2^1 & & \mathbf{B}_n^1 \\ \mathbf{B}_1^2 & \mathbf{B}_2^2 & \ddots & \mathbf{B}_n^2 \\ & & & \\ \mathbf{B}_1^n & \mathbf{B}_2^n & & \mathbf{B}_n^n \end{pmatrix}. \tag{3.9a}$$

where each $\mathbf{B}_j^m$ is an $(l \times l)$ tridiagonal symmetric matrix,

$$\mathbf{B}_j^m = \xi_{jm2}\frac{2a}{b^2}e^{-y^2/b^2}\,\text{tridiag}\left(\frac{y^2}{\Delta y^2}, \frac{-2}{\Delta y^2} - \frac{4y}{b^4} + \frac{6}{b^2} + \lambda_2^2 - \lambda_m^2 - k^2, \frac{y^2}{\Delta y^2}\right) + \beta\mathbf{I}_l, \tag{3.9b}$$

$\mathbf{I}_l$ being the $l \times l$ identity matrix. Writing (3.6) in the following form,

$$c\mathbf{d} = \mathbf{A}^{-1}\mathbf{Bd}, \tag{3.10}$$

the eigenvalues and eigenvectors of the matrix $\mathbf{A}^{-1}\mathbf{B}$ are found by the eigensystem subroutine package EISPACK (Smith et al. 1976).

b. *Numerical results*

To study the linear stability problem, we used a higher meridional resolution, $\Delta y = 1$ km; this does not affect the comparisons with subsequent time-dependent integrations, where $\Delta y = 6$ km. In the parameter range 10 km $< y_0 <$ 100 km of coastal-current width there is only weak dependence of the growth rate on the β effect; this is shown in Table 2 for $u_0 = 6$ cm s^{-1} by comparing e-folding times for $\beta_0 = 1.82 \times 10^{-13}$ cm^{-1} s^{-1} and $\beta_0 = 0$ when using a total of four vertical modes ($0 \leq k \leq 3$). In Table 3 we examine the importance of the β effect for different speeds u_0 of the coastal current, given $y_0 = 50$ km. It is found that only for a weak current, $u_0 < 2$ cm s^{-1}, is the β effect important in determining the growth rate.

The eigenvalue c is almost proportional to a, provided β is not too large, since the elements in matrix $\mathbf{B}$, except $\beta\mathbf{I}$, are proportional to a [cf. Eq. (3.9)]; that is, the growth rate of the most unstable wave and its phase velocity are simply proportional to the maximum speed of the mean current [cf. Eq. (2.6a)]. Thus, in the following we study the instability for the case where $u_0 = 6$ cm s^{-1}; that is, the maximum speed of the

TABLE 2. Dependence of the fastest growing mode of the frontal instability on coastal current width.

y_0 (km)	WL[a] (km)	e-folding time[c] (days)			PV[a] (cm s^{-1})			WP[a] (days)			$-\alpha$ (deg)		
		4[b]	2[b]	$\beta = 0$	4[b]	2[b]	$\beta = 0$	4[b]	2[b]	$\beta = 0$	4[b]	2[b]	$\beta = 0$
100	110	6.1	5.9	5.7	1.1	1.4	1.7	111	92	75	64	62	66
50	110	7.1	6.9	6.9	1.0	1.3	1.3	123	101	95	64	63	67
25	105	9.5	9.1	9.2	0.8	1.1	1.2	153	110	105	63	59	63
10	105	21.8	19.3	20.7	0.6	0.7	0.7	211	182	171	51	52	54

[a] Column headings indicate WL = wavelength, PV = phase velocity, and WP = wave period.
[b] Experiments with $\beta_0 = 1.82 \times 10^{-13}$ cm^{-1} s^{-1} and with four or two vertical modes; the experiments with $\beta = 0$ all use four vertical modes.
[c] Reciprocal of the growth rate.

coastal jet near the sea surface is 20 cm s^{-1}, since $\phi_2(z = 0) = 3.33$.

In Table 2 the wavelength, the *e*-folding time (i.e., the reciprocal of the growth rate), the phase velocity, and wave period of the most unstable wave are listed as a function of y_0 for both the two- and four-mode model (i.e., $k = 0, 1$ and $k = 0, 1, 2, 3$, respectively). The wavelength of the most unstable wave is almost independent of y_0 and the number of modes. The growth rate decreases as the core of the jet, y_0, approaches the coast for two reasons: the baroclinic instability is weakened due to the narrower current while the presence of the coast also tends to suppress the barotropic mode (Ikeda 1983). The wave period is larger by an order of magnitude than the growth rate, that is, we can expect the initial disturbance to grow locally and almost not propagate.

In Fig. 2a the *e*-folding time of the most unstable wave is shown as a function of wavelength. This time has a minimum near 110 km, and increases weakly (strongly) as the wavelength increases (decreases) away from this minimum. In Fig. 2b the real and the imaginary parts of the eigenfunctions D_0 and D_1 are shown for the most unstable wave, and $y_0 = 50$ km. These functions have the most structure in the interval $(0.1y_0, 2.5y_0)$. The extrema of the eigenfunctions obtain at y_0, where the mean current has its maximum.

c. *Barotropic and baroclinic effects*

Looking at the perturbation growth in different modes we notice that the linear growth in the barotropic mode is only due to the (projection on the barotropic mode of the) interaction of the baroclinic perturbation with the mean current, according to the terms

$$\text{BCM} \equiv J(\bar{\psi}, q_j') + J(\psi_j', \bar{q}), \quad j \geq 1 \quad (3.11)$$

in the potential vorticity equation (2.4). The interaction between the barotropic perturbation and the mean current has no direct influence on the barotropic mode.

In the baroclinic mode, the linear growth is due to two pairs of terms:

$$\xi_{111}\{J(\bar{\psi}, q_1') + J(\psi_1', \bar{q})\} = \xi_{111}\text{BCM}, \quad (3.12)$$

that is, (the projection on the first baroclinic mode of) the interaction between the mean current and the baroclinic perturbation, like in the barotropic mode, and

$$\text{BTM} \equiv J(\bar{\psi}, q_0') + J(\psi_0', \bar{q}), \quad (3.13)$$

that is, (the projection on the first baroclinic mode of) the interaction between the barotropic perturbation and the mean current.

The relative importance of the BCM and BTM interaction terms in (3.12) and (3.13), respectively, for the growth of the baroclinic perturbation can be measured by $\tan\alpha$, where α is the phase shift between the perturbation in the (first) baroclinic and the barotropic modes. To show this we can write the perturbation in the barotropic mode at time t as $\psi_0' = E(y)\sin(kx + \gamma)$. Because the wave period is larger by an order of magnitude than the *e*-folding time of the most unstable wave, the functional structure of BCM along the x axis has almost the same form as ψ_0'. Thus, (3.11) and hence (3.12) have both the same sinusoidal x dependence; that is, the sum in (3.12) can be written as $F(y)\sin(kx + \gamma)$. The sum of terms BTM in (3.13) has the functional form $\cos(kx + \gamma)$ along the x axis; that is, it can be written as $G(y)\cos(kx + \gamma)$. Thus,

$$\frac{\partial q_1'}{\partial t} = F(y)\sin(kx + \gamma) + G(y)\cos(kx + \gamma)$$
$$= H(y)\sin(kx + \gamma + \alpha), \quad (3.14)$$

TABLE 3. Dependence of the fastest instability's *e*-folding time on velocity and β effect. Four vertical modes, one barotropic and three baroclinic, are used.

u_0 (cm s^{-1})	e-folding time (days)	
	$\beta_0 = 1.82 \times 10^{-13}$ (cm^{-1} s^{-1})	$\beta_0 = 0$
1	54.3	41.6
2	23.1	20.8
3	14.8	13.9
4	10.9	10.4
6	7.1	6.9

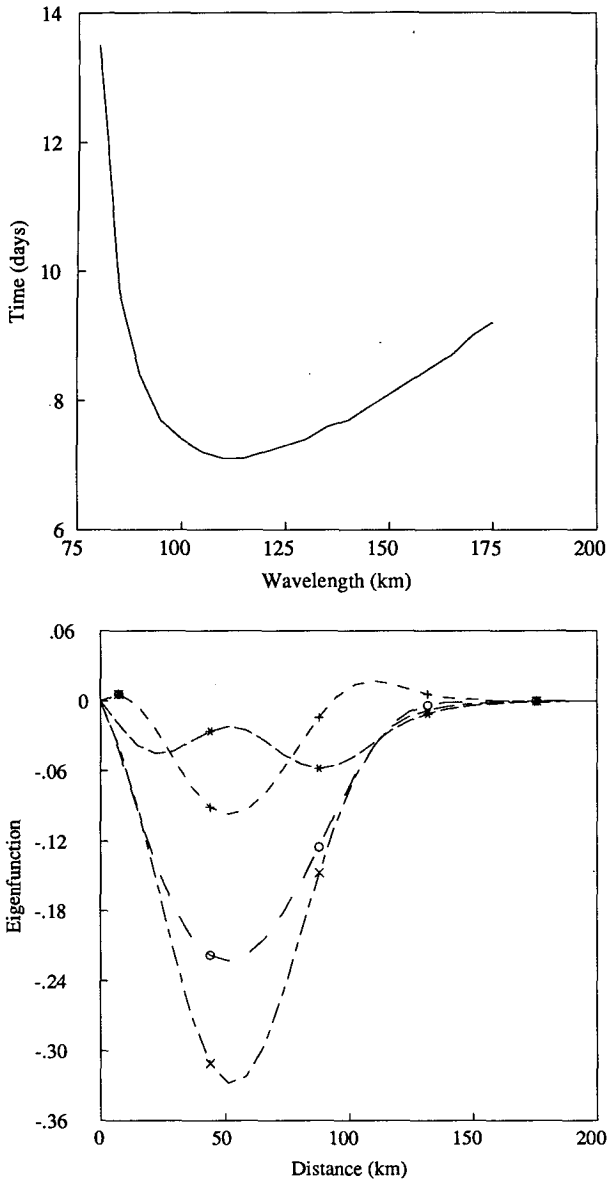

FIG. 2. (a) The minimum e-folding time, corresponding to the maximum growth rate, as a function of wavelength, for $y_0 = 50$ km and $u_0 = 6$ cm s^{-1}. (b) The real and imaginary parts of the eigenfunctions D_0 and D_1 in this case: (× with long-short dashes) real part of D_0; (* with long dashes) imaginary part of D_0; (+ with short dashes) real part of D_1; (○ with long dashes) imaginary part of D_1.

that is,

$$F(y) = H(y)\cos\alpha, \quad G(y) = H(y)\sin\alpha,$$
$$\tan\alpha = G(y)/F(y). \qquad (3.15a\text{-}c)$$

In Table 2 the values of α are given for the most unstable wave in the interval $y_0/10 \leq y \leq 2y_0$. In this interval the value of α is almost constant. In the case where $y_0 = 50$ km and $\tan\alpha = 2.0$, we can conclude that the perturbation growth in the first baroclinic mode is mainly due to the interaction between the barotropic mode and the mean current.

In summary, the linear growth of the perturbation in the barotropic mode is due to (the projection on the barotropic mode of) the across-shore advection of the mean current's potential vorticity by the baroclinic perturbation [cf. (3.11)]. The linear growth in the (first) baroclinic mode is mainly due to the across-shore advection of the mean current's potential vorticity, and hence streamlines, by the barotropic perturbation [cf. (3.12)–(3.15)].

This kind of advection can be seen by superimposing the streamfunction of the first baroclinic mode, shown in Fig. 3, on the barotropic streamfunction of Fig. 4 at $t = \tau$. Our basic time unit in describing the subsequent experiments will be $\tau \equiv 160\Delta t = 2.16$; dimensionally, $\tau = 5$ days.

The troughs and the ridges of the baroclinic mode are located between the troughs and the ridges of the barotropic mode, as $50° \leq \alpha \leq 70°$ in Table 2. The troughs ($\mathbf{t}^n$, $n = 1, 2, 3$) and ridges ($\mathbf{r}^n$, $n = 1, 2$) of the baroclinic mode (Fig. 3) are amplified by the advection of the streamlines of the mean current due to the flow perpendicular to the coast generated by the barotropic mode's closed high ($\mathbf{H}^n$, $n = 1, 2, 3$) and low ($\mathbf{L}^n$, $n = 1, 2, 3$) cells (Fig. 4). For instance, the onshore flow generated between $\mathbf{H}^1$ and $\mathbf{L}^1$ (Fig. 4b) reinforces the trough $\mathbf{t}^1$ (Fig. 3b), and the offshore flow between $\mathbf{L}^1$ and $\mathbf{H}^2$ reinforces the ridge $\mathbf{r}^1$.

4. Eddy formation

The analysis in sections 3b and 3c applies only to the first stage of the evolution, when the amplitude of the unstable waves is small. Later on, as the amplitude of the perturbations grows, the nonlinear interaction between the waves dominates the formation and subsequent evolution of the eddies. We proceed to examine this evolution with the numerical model. The initial perturbation for the basic experiment has the form

$$\psi'(x, y, z, 0) = \begin{cases} d\sin(kx)\phi_1(z), & 720 \text{ km} < xL < 996 \text{ km}, \\ & -144 \text{ km} < yL < -24 \text{ km}, \\ 0, \quad \text{otherwise}; \end{cases} \qquad (4.1)$$

here $2\pi/k = 130$ km$/L$, $d = 1/(Vk)$ and ψ' is superimposed on the coastal jet given by (2.5). We choose this wavelength since its growth rate is almost the same as that of the most unstable wave (Fig. 2). In Fig. 3a this initial current and perturbation are shown at $t = 0$. A short time after the start of the simulation the perturbation that grows and becomes dominant has the same y dependence in all modes as the solution of (3.10). In Figs. 3b and 4b this can be seen at $t = \tau$ for modes $j = 0$ and 1. The amplitude of modes 2 and 3

is smaller by an order of magnitude, and their structure (not shown) is similar to mode 0.

a. Evolution of the first baroclinic mode

To simplify the description, we denote the initial ridges by $\mathbf{r}^1$ and $\mathbf{r}^2$ and the troughs by $\mathbf{t}^1$, $\mathbf{t}^2$, and $\mathbf{t}^3$ (indices increase from east to west). Until $t = 4\tau$, the linear growth of the initial perturbation is the dominant feature. Later on, between $t = 4\tau$ and 6τ (Figs. 3c,d), we observe the following four main tendencies. (i) In the troughs ($\mathbf{t}^1$–$\mathbf{t}^3$) the streamlines stretch near the coast, while in the ridges $\mathbf{r}^1$–$\mathbf{r}^3$ the streamlines stretch in the open sea. (ii) The streamlines tilt onshore toward the west in the troughs, with the larger tilt in their western part, while they tilt offshore toward the east in the ridges, with the larger tilt in their eastern part. (iii) The entire system of troughs and ridges propagates toward the west; largest amplitudes are at the eastern end of the wave train, and new features arise, with small amplitude initially, at the western end. (iv) As the perturbations grow, the mean current near the coast is essentially suppressed by the trapping of the streamlines into the eddies.

The first two tendencies lead to closing of the ridges near the coast and formation of anticyclonic eddies in the open sea, on the one hand, and closing of the troughs in the open sea and formation of cyclonic eddies near the coast, on the other. The first tendency is due to the advection of the baroclinic-mode streamlines by the barotropic flow, as shown forthwith. The argument is a mere refinement of the one given in the last paragraph of section 3c.

Indeed, pairs of $\mathbf{H}^n$ and $\mathbf{L}^n$ cells in the barotropic mode (Fig. 4) have convergence of onshore flow from seaward to about 50 km off the coast (i.e., the distance of the cell centers from the coast) and divergence from that point on to the coast. This stretches the baroclinic troughs (Fig. 3) in the alongshore direction near the coast. Conversely, offshore flow between $\mathbf{L}^n$ and $\mathbf{H}^{n+1}$ converges between the coast and the line of cell centers, and diverges from there on seaward, thus stretching the baroclinic ridges in their open-sea part, also in the alongshore direction. Alongshore contraction of the streamlines near the coast in the ridges and in the open sea for the troughs follows obviously from the above.

The second tendency, that is, the tilting of the streamlines in the first baroclinic mode, is likewise a higher-order result of the phase shift, α, between the waves of the barotropic and the first baroclinic mode, as discussed also in section 3c. The weakly nonlinear consequences of this phase shift are as follows. The ridges of the first baroclinic mode overlap a larger part of the cyclonic (**L**) cell in the barotropic mode than of the anticyclonic (**H**) cell, and the troughs of the former overlap a larger part of the anticyclonic (**H**) cell in the latter. Thus, the advection of the ridges of the first baroclinic mode by the barotropic mode in the open sea is more pronounced in their eastern part than in the west, while the advection of the troughs of the baroclinic mode by the barotropic mode near the coast is more pronounced in their western part.

The westward propagation and downstream development of the system is due to the interaction of the first baroclinic mode with itself and to the linear β term.

The aforementioned tendencies can be explained by examining the different terms in the equation for the streamfunction of the first baroclinic mode in (2.4):

$$\frac{\partial \psi_1}{\partial t} = -\beta L_1 \beta \frac{\partial \psi_1}{\partial x} - L_1[J(\psi_0, q_1) + J(\psi_1, q_0)] - \xi_{111} L_1 J(\psi_1, q_1) - L_1\Big[\sum_{\substack{j=0 \\ (j+l>1, j\neq l)}}^{3}\sum_{l=0}^{3} \xi_{1jl} J(\psi_j, q_l)\Big], \tag{4.2}$$

where L_j is the inverse Helmholtz operator for mode j,

$$L_j = (\nabla^2 - \lambda_j)^{-1}. \tag{4.3}$$

Tendencies (i) and (ii) are due to the interaction terms between the barotropic and the first baroclinic mode:

$$-L_1[J(\psi_0, q_1) + J(\psi_1, q_0)]. \tag{4.4}$$

In Fig. 5a, this sum is shown at $t = 4\tau$. Superimposing the structure of the H and L cells in this figure on Fig. 3c shows both of the aforementioned tendencies.

The third tendency is due to the two terms

$$-\xi_{111} L_1 J(\psi_1, q_1) - \beta L_1 \frac{\partial \psi_1}{\partial x}. \tag{4.5}$$

In Fig. 6 the sum of these two terms is shown at $t = 4\tau$. Superposition of this figure on Fig. 3c shows clearly both the westward propagation and the downstream development. The other terms in (4.2) are much smaller and at this stage can be neglected.

At $t = 7\tau$ (Fig. 3e) the ridges $\mathbf{r}^2$ and $\mathbf{r}^3$ [the latter having developed by $t = 4\tau$ (Fig. 3c)] have evolved into anticyclonic eddies. In the time interval $8\tau \leq t \leq 12\tau$ (Figs. 3f–j), $\mathbf{r}^2$ propagates toward the southwest. Eddy $\mathbf{r}^3$ propagates toward the northeast until it reaches the coast (Figs. 3f–h), after which it propagates westward along the coastline.

In the time interval $7\tau \leq t \leq 9\tau$ (Figs. 3e–g) the new ridge $\mathbf{r}^4$ evolves into an anticyclonic eddy. From then on until $t = 12\tau$ (Figs. 3h–j), this eddy propagates toward the southeast. In the time interval $9\tau \leq t \leq 12\tau$ (Figs. 3g–j) the anticyclonic eddy $\mathbf{r}^5$ is also formed and propagates toward the southeast.

The cyclonic eddies that evolve from the troughs $\mathbf{t}^1$–$\mathbf{t}^3$ live but for a short time, as they are pushed toward the coast and spread out along it. These eddies then merge and form a very narrow and rapid current along the coast. The dissipation of that current by the friction with the coast cannot be simulated adequately with a

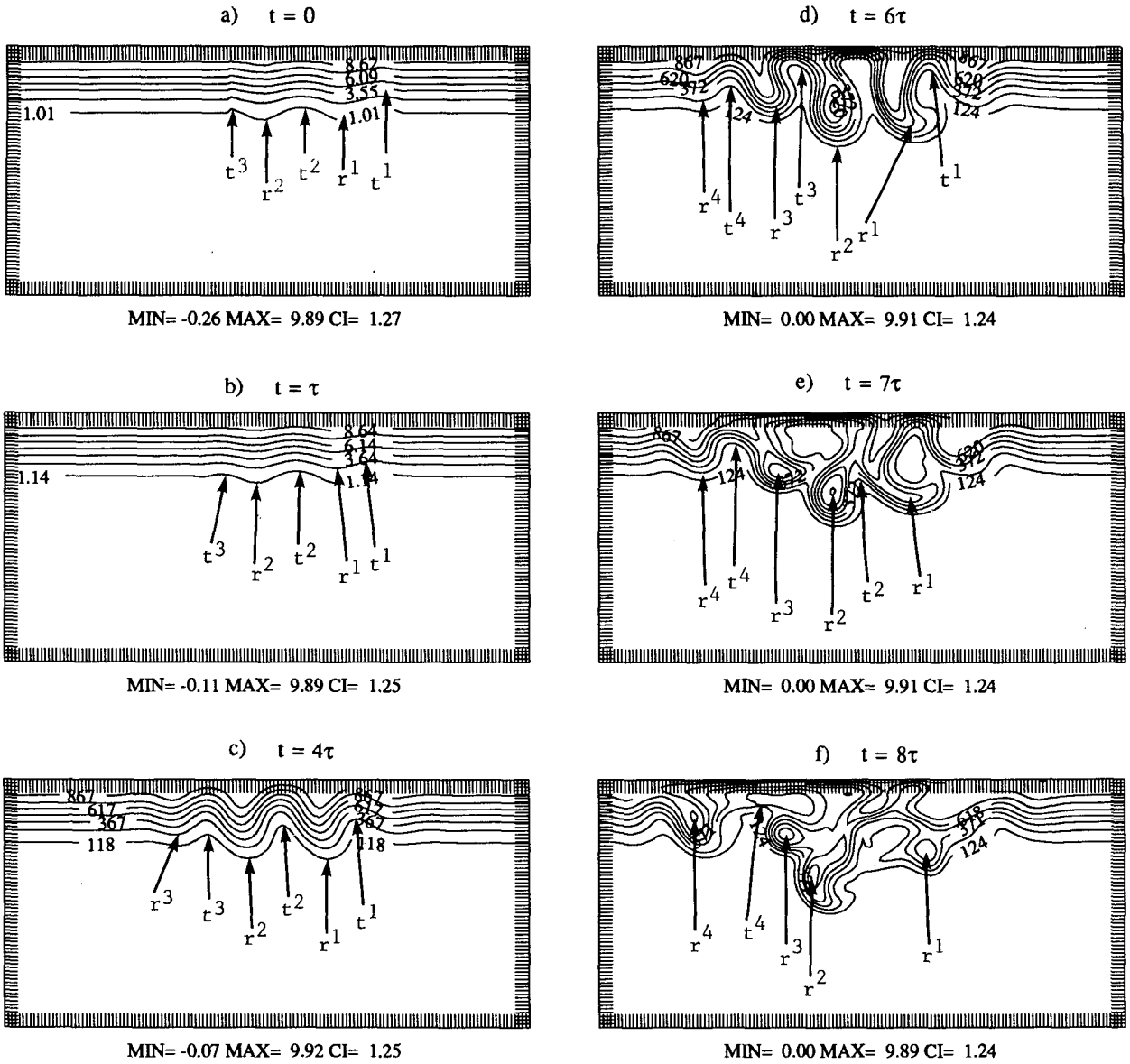

FIG. 3.

quasigeostrophic model, which requires the coast to be represented by a constant value of the streamfunction. Increasing the diffusion in the model [cf. (2.7)], will act however to increase the width and reduce the intensity of the current.

The propagation of the anticyclonic eddies $\mathbf{r}^2$–$\mathbf{r}^5$ is mainly due to their advection by the barotropic flow. Each baroclinic eddy overlaps a barotropic dipole. This dipole advects the eddy riding over it along the observed propagation track of the latter. This can be seen by considering the interaction term between the second and first mode, Eq. (4.4). In Fig. 5b this term is shown at $t = 10\tau$; at later times (not shown) it has similar features. Superimposing this figure on Fig. 3h, the advection of the eddies $\mathbf{r}^2$–$\mathbf{r}^5$ is clearly apparent. The other terms in (4.2) are smaller by at least a factor of 5 in the eddies.

The meandering of the model's mean current amplifies, and eddies detach after about 3τ time units or, in dimensional units, about 15 days. Some of the eddies ($\mathbf{r}^2$, $\mathbf{r}^4$, and $\mathbf{r}^5$) propagate away from the coast, some ($\mathbf{r}^3$) toward the coast, and the position of one ($\mathbf{r}^1$) seems to oscillate back and forth.

There are noteworthy similarities between the eddies obtained in the numerical simulation here and the observed anticyclonic eddies in the Eastern Mediterranean. First, the radii of both observed and simulated eddies (Feliks and Itzikowitz 1987; Ozsoy et al. 1989) are between 35 and 50 km. Furthermore, Ozsoy et al. (1989) observed simultaneously a series of three an-

g) t = 9τ

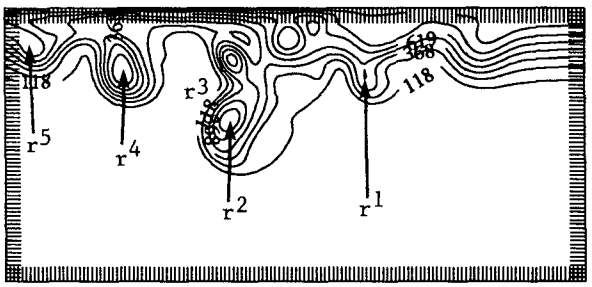

MIN= -0.08 MAX= 9.95 CI= 1.25

h) t = 10τ

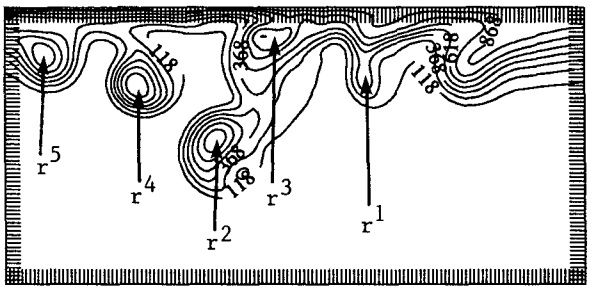

MIN= -0.07 MAX= 9.94 CI= 1.25

i) t = 11τ

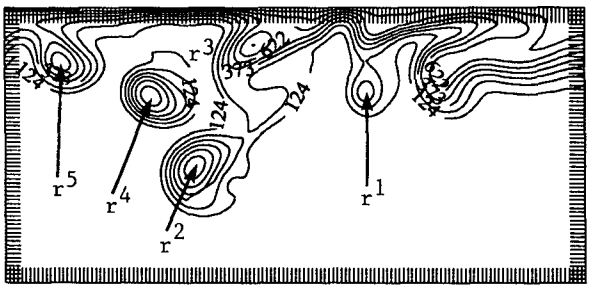

MIN= -0.01 MAX= 9.95 CI= 1.24

j) t = 12τ

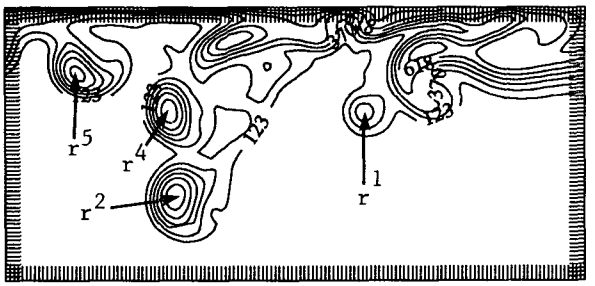

MIN= -0.01 MAX= 9.89 CI= 1.24

FIG. 3. The streamfunction of the first baroclinic mode at successive times in the subdomain 354 km $< x <$ 1194 km, -174 km $< y < 0$ km. Each panel shows the minimum (MIN) and maximum (MAX) value of the streamfunction contoured and the contour interval (CI).

ticyclonic eddies along the northeastern coast of the Eastern Mediterranean, which—in their terminology—"masked" the Asia Minor current. In our simulation, several anticyclonic eddies were observed at the same time along the coast and persisted jointly for a simulated month or more. In both observations and simulation, the mean current is not noticeable along the coast, while the eddies are forming near and moving away from it.

Finally, the density field in the observed and simulated eddies is very similar. Indeed, the horizontal structure of the density deviation $\delta_j(x, y, t)$ from the mean—in x, y, and t—of the density in mode j is the same as the streamfunction of that mode [see Eq. (2.3a)] in the quasigeostrophic model:

$$\delta(x, y, z, t) = \sum_{j \geq 1} \psi_j(x, y, t) \frac{\partial \phi_j(z)}{\partial z}. \quad (4.6)$$

Since the basic jet (2.5) describes well the density of the downwelling front (Feliks 1991, his Figs. 4 and 5), the density deviation of the first baroclinic mode in the core of eddies $\mathbf{r}^2$ and $\mathbf{r}^3$ equals that of the observed front about 15 km off the coast, which equals in turn that of the observed anticyclonic eddies in the northeastern Mediterranean (Feliks 1991, his Fig. 9).

b. *Evolution of the barotropic mode*

In the time interval $0 \leq t \leq 4\tau$ the evolution in the barotropic mode (Figs. 4a–c) is mainly due to linear

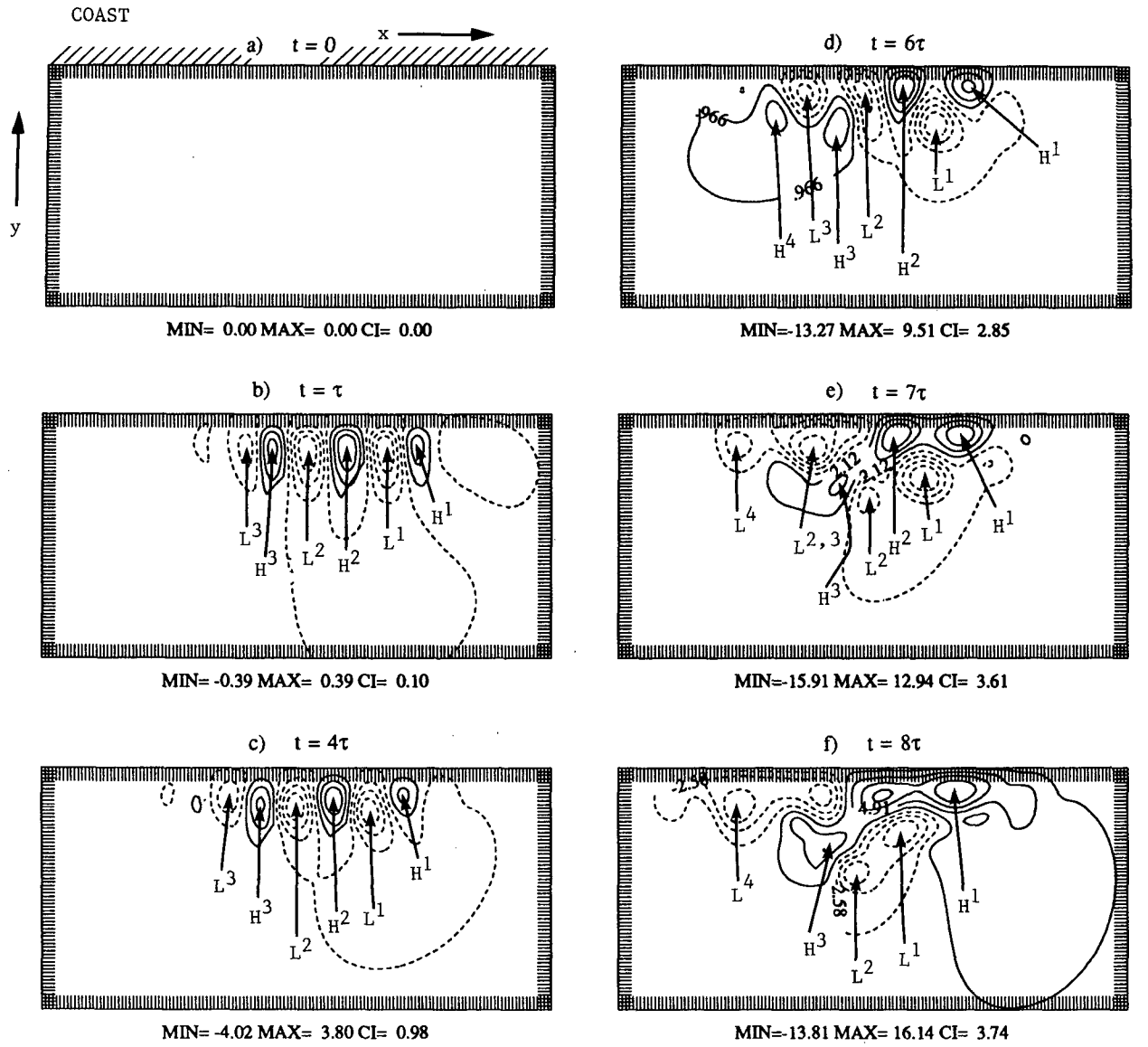

FIG. 4.

instability and is discussed in section 3c. To simplify the description of the nonlinear effects, we denote the anticyclonic cells by $\mathbf{H}^1$–$\mathbf{H}^4$ and the cyclonic cells by $\mathbf{L}^1$–$\mathbf{L}^3$; the indices increase from east to west, as in the previous subsection.

In the time interval $4\tau \leqslant t \leqslant 8\tau$ the main tendencies observed in the barotropic mode are as follows. (i) $\mathbf{H}^1$, $\mathbf{H}^2$, $\mathbf{L}^2$, and $\mathbf{L}^3$ are pushed toward the coast, while $\mathbf{L}^1$, $\mathbf{H}^3$ and the northern part of $\mathbf{L}^2$ move away from the coast. (ii) $\mathbf{H}^1$ and $\mathbf{H}^2$ merge and evolve into a larger anticyclonic eddy, while $\mathbf{L}^3$ and part of $\mathbf{L}^2$ merge and evolve into a larger cyclonic eddy. These large cyclonic and anticyclonic eddies are elongated along the shoreline. (iii) $\mathbf{H}^1$, $\mathbf{L}^1$, $\mathbf{H}^2$, and $\mathbf{L}^2$ all propagate westward. (iv) The amplitude of the cyclonic and anticyclonic cells continues to grow.

These tendencies can be explained by examining the different terms in the equation for the barotropic streamfunction (2.4):

$$\frac{\partial \psi_0}{\partial t} = -\beta L_0 \frac{\partial \psi_0}{\partial x} - L_0 J(\psi_0, q_0) - L_0 J(\psi_1, q_1) - \sum_{j \geqslant 2} L_0 J(\psi_j, q_j), \quad (4.7)$$

with L_j as defined in (4.3).

Tendencies (i), (iii), and (iv) are due in part to the term $-L_0 J(\psi_1, q_1)$. In Fig. 7 this term is shown at t

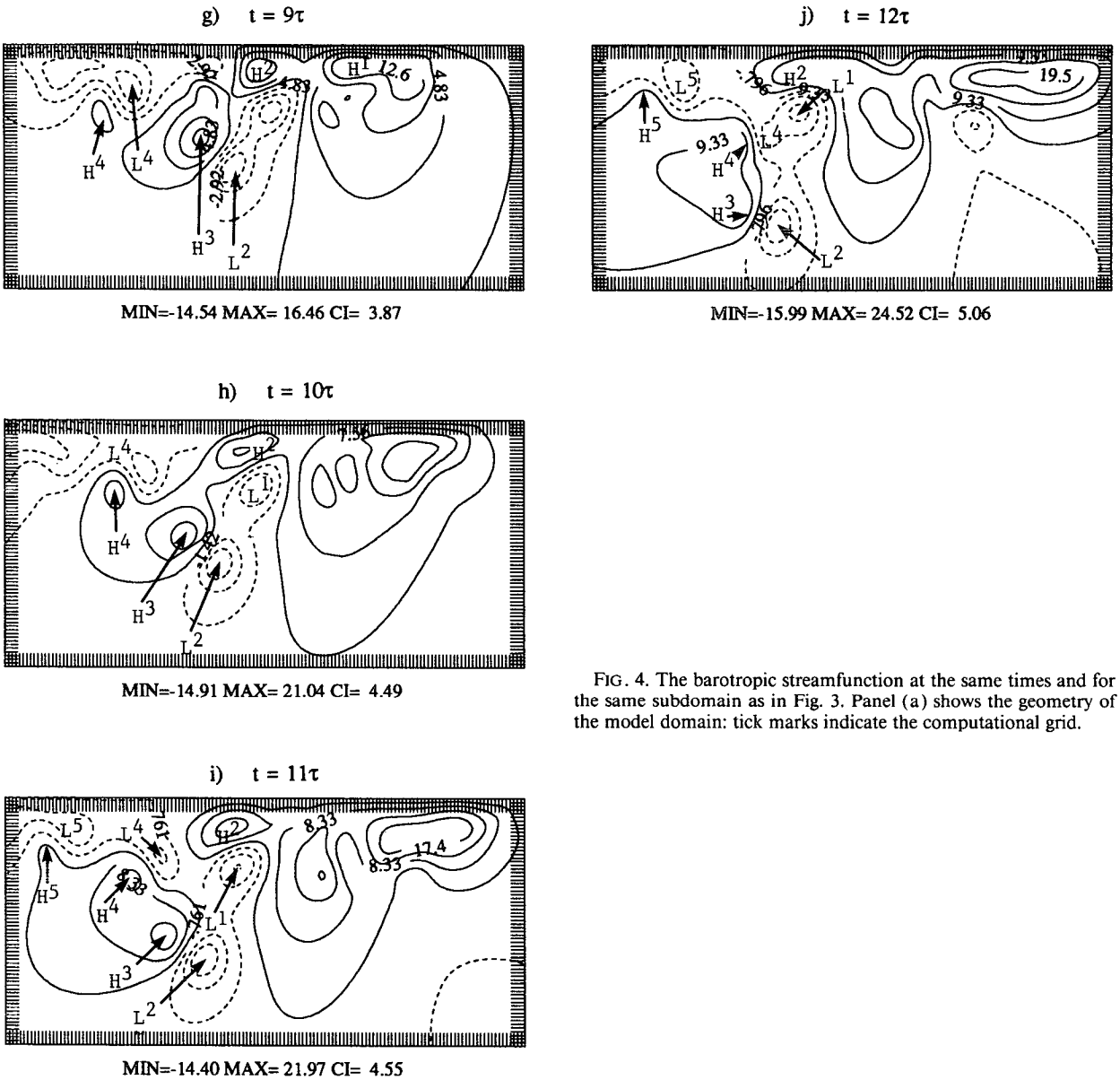

FIG. 4. The barotropic streamfunction at the same times and for the same subdomain as in Fig. 3. Panel (a) shows the geometry of the model domain: tick marks indicate the computational grid.

$= 6\tau$. Tendency (ii) and the other tendencies that determine the movement of $\mathbf{H}^1$, $\mathbf{L}^1$, $\mathbf{H}^3$, and $\mathbf{L}^3$ are also due to the term $-L_0J(\psi_0, q_0)$. In Fig. 8a this term is shown at $t = 6\tau$.

From $t = 7\tau$ (Fig. 4e) on, two dipoles, $\mathbf{L}^2$–$\mathbf{H}^3$ and $\mathbf{L}^1$–$\mathbf{H}^2$, form and persist. The dipole $\mathbf{L}^2$–$\mathbf{H}^3$ moves southwestward, while the dipole $\mathbf{L}^1$–$\mathbf{H}^2$ moves very slowly westward. Another dipole evolves from the cells $\mathbf{L}^4$–$\mathbf{H}^4$. This dipole moves toward the southeast. The movement of the dipoles is mainly due to the term $-L_0J(\psi_0, q_0)$; that is, their propagation is due to self-advection (see Fig. 8b at $t = 10\tau$; at later times—not shown—the pattern is similar). The term $-L_0J(\psi_1, q_1)$ tends to rotate the dipoles $\mathbf{L}^2$–$\mathbf{H}^3$ and $\mathbf{L}^1$–$\mathbf{H}^2$ in the clockwise direction and the dipole $\mathbf{L}^4$–$\mathbf{H}^4$ in the opposite direction, against the tendency of other terms in Eq. (4.7).

There is an analogy between the self-advection of barotropic dipoles in this subsection and the passive advection of baroclinic monopoles in the previous one, on the one hand, with the known propagation properties of barotropic modons with passive baroclinic riders, on the other. The track of the barotropic dipoles here is mainly determined by the nonlinear advection terms and the linear β term, like for classical modons. This adds coastal current instability to the list of po-

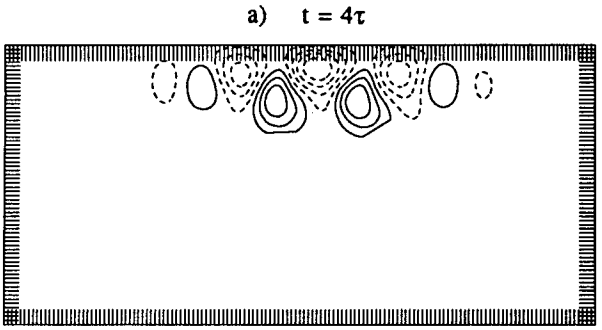

FIG. 5. The tendency term (4.4) at (a) $t = 4\tau$ and (b) $t = 10\tau$ in the same subdomain as in Fig. 3.

tentially important formation mechanisms for modon–rider systems in the ocean. The scarcity of data on the Anatolian Current and its instabilities, however, does not permit definitive confirmation of this heuristic hypothesis by a study of the detailed dispersion relations of the perturbations' barotropic and baroclinic components, as done for some of the other formation mechanisms (McWilliams and Flierl 1979; Mied and Lindemann 1982; Feliks 1990).

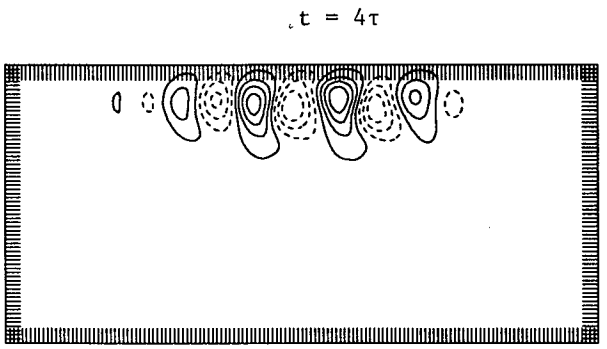

FIG. 6. The tendency term (4.5) at $t = 4\tau$ in the same subdomain as in Fig. 3.

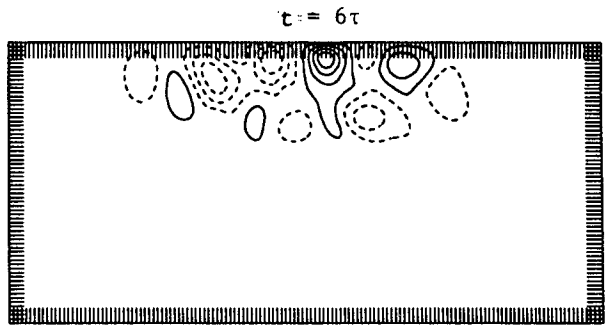

FIG. 7. The tendency term $-L_0J(\psi_1, q_1)$ at $t = 6\tau$ in the same subdomain as in Fig. 3.

c. Energy

The available potential energy (APE) of mode k is $\mathrm{APE}_k = \lambda_k^2\psi_k^2$, and the kinetic energy (KE) of mode k is $\mathrm{KE}_k = (\partial\psi_k/\partial x)^2 + (\partial\psi_k/\partial y)^2$. In Fig. 9 the integrals over the entire domain of $\mathrm{KE}_0(t)$ and $\mathrm{KE}_1(t)$–$\mathrm{KE}_1(0)$ are shown. The growth of kinetic energy in the barotropic mode is three to four times larger than in the first baroclinic mode. This result can be interpreted to

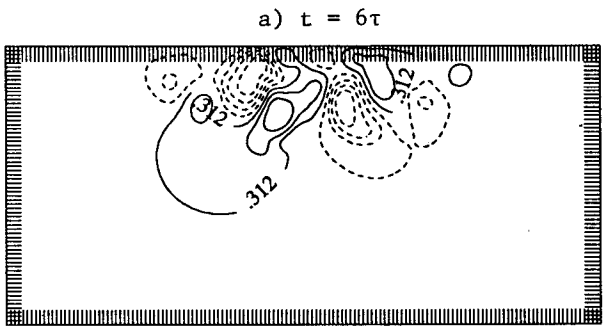

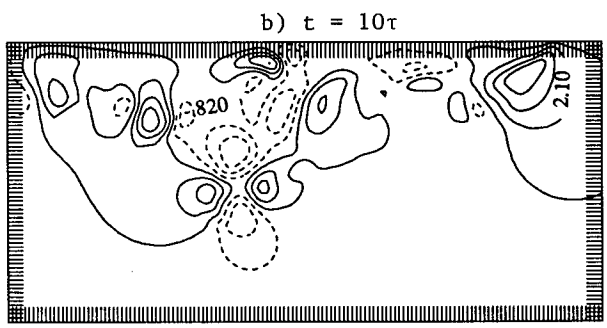

FIG. 8. The barotropic tendency term $-L_0J(\psi_0, q_0)$ at (a) $t = 6\tau$ and (b) $t = 10\tau$ in the same subdomain as in Fig. 3.

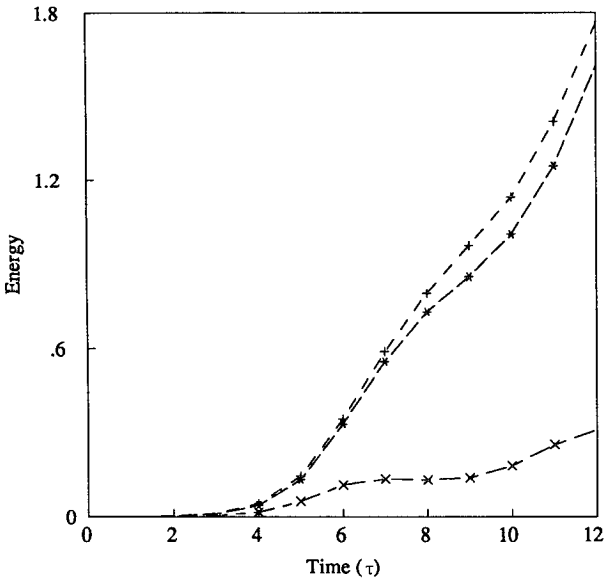

FIG. 9. The integral over the model domain of: (× with long dashes) the kinetic energy of the first baroclinic mode as a function of time, $\int\int (\mathrm{KE}_1(x, y, t) - \mathrm{KE}_1(x, y, 0))dxdy$; (+ with short dashes) the energy transfer between this mode and the barotropic one as a function of time, $\int\int \mathrm{ET}_{01}(x, y, t)dxdydt$; (∗ with long dashes) the kinetic energy of the barotropic mode as a function of time, $\int\int \mathrm{KE}_0(x, y, t)dxdy$.

imply that 80% of the part of APE_1 that is transferred to kinetic energy contributes to the barotropic mode.

An expression for the energy transfer between the different modes is obtained by multiplying Eq. (2.4) by ψ_k. It follows that the energy transfer rate from mode i to mode k is

$$\mathrm{ET}_{ki}(x, y, t) = \psi_k \sum_j \xi_{ijk}[J(\psi_i, q_j) + J(\psi_j, q_i)]\,. \tag{4.8}$$

The energy transfer rate from mode 1 to mode 0 is, therewith,

$$\mathrm{ET}_{01}(x, y, t) = \psi_0 \xi_{011} J(\psi_1, q_1). \tag{4.9}$$

From Fig. 9 we see that the large transfer toward the barotropic mode, Eq. (4.9), explains the accumulation of energy KE_0 in this mode. The energy growth in the barotropic mode is significantly faster after $t = 4\tau$ than before, due to the larger energy transfer toward it from $t = 4\tau$ on; nonlinear interactions seem to enhance the transfer substantially. The difference between the energy transferred to the barotropic mode and the energy residing in this mode is due to dissipative losses introduced by the filtering process [cf. Eq. (2.7)].

To provide more spatial detail on the energy transfer rate, we show in Fig. 10 maps of ET_{10} at different times over the same subdomain as in Figs. 3 and 4. The transfer rate in the ridges $\mathbf{r}^2$–$\mathbf{r}^4$ increases slowly during the linear growth stage, up to $t = 4\tau$ (Fig. 10a). During eddy formation, ET_{10} increases rapidly (Fig. 10b). After eddy detachment, this energy transfer decreases (Fig. 10c). For the eddy $\mathbf{r}^2$, the transfer rate reaches its maximum at $t = 8\tau$. At $t = 11\tau$, the energy transfer is small and occurs in both directions (Fig. 10c). Along the coast large energy transfers are observed at all times.

Comparing Fig. 10 with Figs. 3 and 4, we notice that the energy transfer toward the barotropic mode has much smaller scale than the flow in either the baroclinic or the barotropic mode. The growth of the scale of the

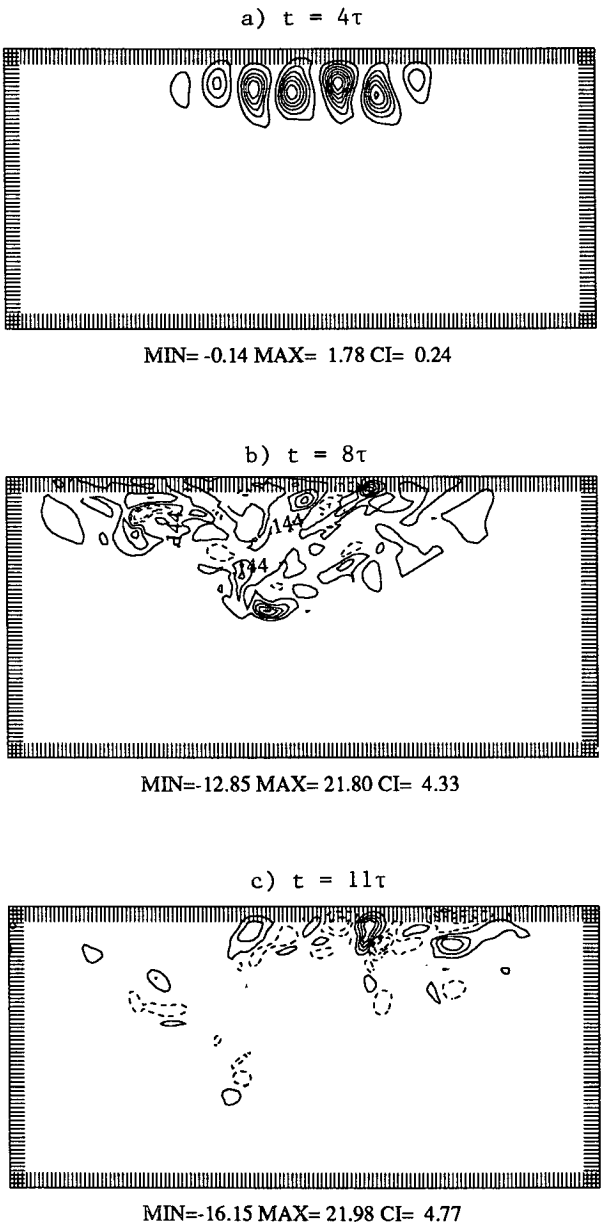

FIG. 10. The energy transfer rate between the barotropic and the first baroclinic modes in the same subdomain as in Fig. 3: (a) $t = 4\tau$, (b) $t = 8\tau$, and (c) $t = 11\tau$.

motion in the barotropic mode can be understood in terms of the nearly two-dimensional character of quasigeostrophic turbulence; that is, the energy in the barotropic mode tends to cascade toward the larger scales (Charney 1971).

The energy in modes 2 and 3 is smaller by two orders of magnitude than in modes 0 and 1. This small transfer of energy toward the higher baroclinic modes compared to that toward the barotropic mode may result from a related property of quasigeostrophic turbulence, namely, that energy tends to cascade toward the larger total scale; that is, most of the energy will cascade to the lower vertical modes (Rhines 1977; Salmon 1978; Fu and Flierl 1980; Feliks 1990).

5. Parametric dependence

To verify the robustness of the results reported in section 4, a number of additional experiments, aside from the basic one described there, have been carried out. They include changes in the β effect, the number of vertical modes, the horizontal resolution, and the width of the coastal jet.

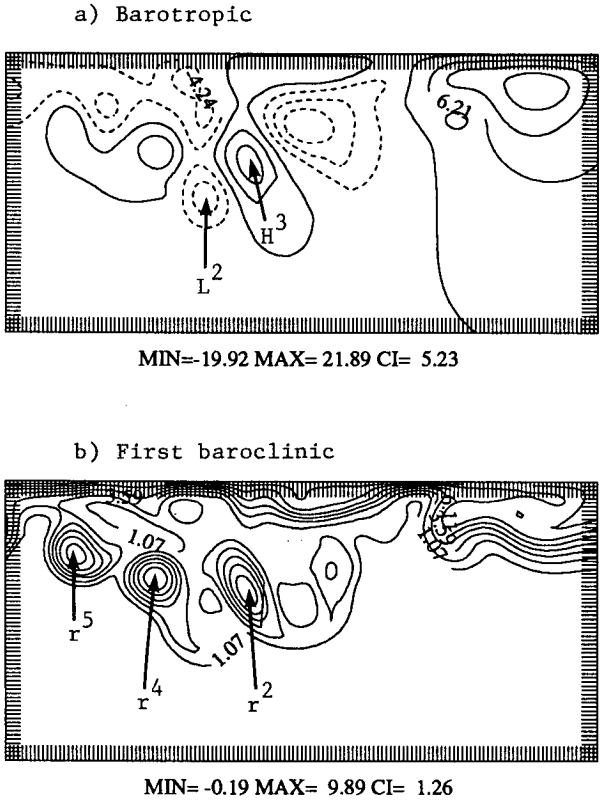

FIG. 11. The streamfunction for an experiment with $\beta = 0$: (a) the barotropic mode; (b) the first baroclinic mode. The subdomain is the same as in Fig. 3, and $t = 12\tau$.

a. *The β effect*

To examine the importance of the β effect for the previous results, β was set to zero. In section 3b we found that the β effect was negligible for the linear instability of the westward jet, except for very small u_0 (see Table 3). The results of the numerical simulation confirm this: only after eddies develop do significant differences between the two experiments appear. In the first baroclinic mode (Fig. 11b) the prominent differences are in the propagation track of the eddies: when $\beta = 0$, $\mathbf{r}^2$ is displaced much less toward the southwest from where it arises; $\mathbf{r}^4$ is formed farther west than in the basic experiment (Fig. 3j) and moves a larger distance to the east. The largest differences between the two experiments are observed in the position of $\mathbf{r}^2$, since it forms before the other eddies do. The westward acceleration due to the β effect for southward displacements explains the differences in zonal propagation between the two experiments. The differences in southward propagation are discussed forthwith.

In the barotropic mode the main difference is that when $\beta = 0$ (Fig. 11a) the cell $\mathbf{L}^2$ rotates around the cell $\mathbf{H}^3$. So at $t = 12\tau$, $\mathbf{L}^2$ is west of $\mathbf{H}^3$, while in the basic experiment the pole $\mathbf{L}^2$ is always east of $\mathbf{H}^3$. This difference in the position of the dipole $\mathbf{H}^3$–$\mathbf{L}^2$ causes the slower southward propagation of the baroclinic rider $\mathbf{r}^2$ in the present experiment.

b. *Number of modes*

In the linear analysis of section 3b, we found that there is only a small difference in any property of the most unstable wave (see Table 2) between the model with two or four vertical modes. We saw furthermore in the basic experiment of section 4 that the higher baroclinic modes contained very little energy.

Therefore, we integrated Eq. (2.4) with only two vertical modes, one barotropic and one baroclinic. Until $t = 9\tau$ the differences between the basic and the present experiment are very small. Later on, as we might have surmised from the results of Feliks (1990), larger differences begin to appear. The main differences are (i) the initial ridge $\mathbf{r}^1$ develops into an eddy only in the two-mode experiment (Fig. 12b); (ii) the anticyclonic eddy $\mathbf{r}^2$ and the barotropic dipole $\mathbf{L}^2$–$\mathbf{H}^3$ (Fig. 12a) in this experiment propagate toward the southeast, while in Figs. 3 and 4 they propagate toward the southwest; and (iii) the barotropic dipole $\mathbf{L}^2$–$\mathbf{H}^3$ (Fig. 12a) in the two-mode experiment has orientation—defined as the direction of the normal to the axis that connects the two poles, with the cyclonic one to the left of the oriented normal, that is, the direction of motion of the dipole under its own velocity field—toward the southeast, while in the four-mode experiment its orientation is toward the southwest. This difference in the orientation of the dipole explains difference (ii), since the

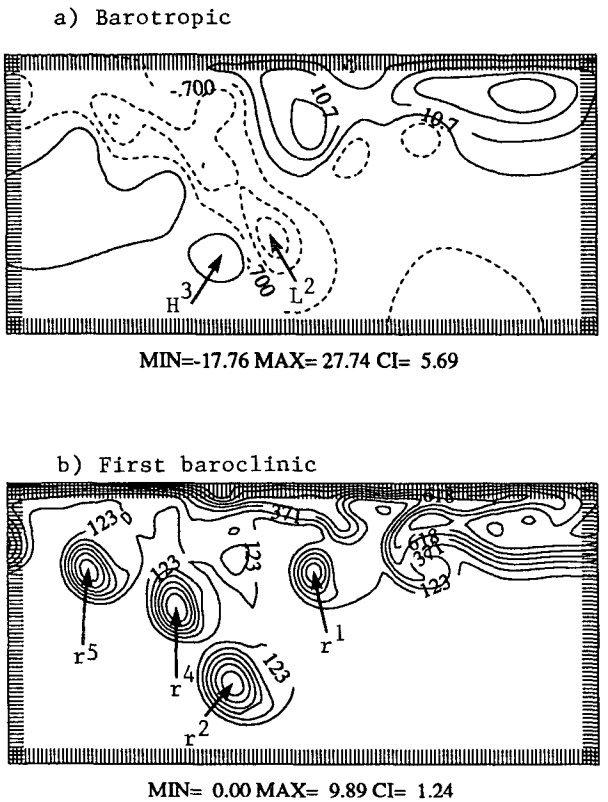

FIG. 12. The streamfunction for an experiment with two vertical modes only: (a) the barotropic mode; (b) the first baroclinic mode. Same time and subdomain as in Fig. 11.

joint propagation of the dipole and its rider is mainly due to advection by the dipole, as shown in section 4.

c. *The horizontal resolution*

Since the horizontal resolution in the previous experiments was $\Delta x = \Delta y = 6$ km/L, that is, larger than the deformation radii of the second and third baroclinic modes, we examine in this subsection the evolution for both a two- and a four-mode model when the spatial resolution is $\Delta x = \Delta y = 2$ km/L and the time step is $\Delta t = 1350\text{ s} \div T$. We use the same fourth-order Shapiro (1970) filter every time step. The integration domain in the following simulations was of 513 × 193 grid points or 1026 km × 386 km; this is slightly smaller, for reasons of computational efficiency, than the domain of section 4, with 1464 km × 582 km. The initial data were the same as in the previous experiments, and the integration was carried out until $t = 9\tau$; up to this time, no significant interaction occurs between the eddies and the computational boundaries in the domain chosen here.

In the four-mode model the energy in modes 2 and 3 is still smaller by two orders of magnitude than in modes 0 and 1. This result is the same as for the coarser grid, being an intrinsic property of quasigeostrophic turbulence (see section 4c), not affected unduly by the horizontal resolution.

Comparing the two- and four-mode simulations, we find that until $t = 9\tau$ there were no significant differences. We conclude that for short times the two-mode model is as good as the four-mode model in cases when the initial mean current is in the first baroclinic mode.

The four-mode model simulations on different grids, that is, $\Delta x = \Delta y = 2$ and 6 km/L, exhibit a very similar evolution. The only difference is that on the coarser grid the eddies are more diffuse, since the fourth-order filter causes larger dissipation there. Indeed, given the temporal and spatial resolution used in the high- and low-resolution experiments, the diffusion coefficient A in Eq. (2.7) is about 40 times larger on the coarse grid than on the fine grid. This explanation of the difference was confirmed by running the model on the coarser grid with an eighth-order Shapiro filter. In the latter simulation the eddies are less diffuse and very similar to those obtained in the fine-grid simulation with the fourth-order filter.

d. *The width of the jet*

Feliks (1991) showed that the across-shore scale of the jet is proportional to the square root of the horizontal diffusion coefficient. Due to uncertainty in the value of that coefficient, the horizontal scale of the jet, defined as the distance between the coast and the location of the maximum speed in the jet, is also uncertain. In this subsection we examine the eddy formation given a different jet width; that is, the maximum speed of the jet occurs at $y_0 = 25$ km off the coast. Since we assume that the downwelling near the coast has penetrated to the same depth in both cases, the value of the streamfunction near the coast must be the same. Thus, according to (2.6a), the maximum speed of the jet is twice that of the basic experiment; that is, $u_0 = 12$ cm s^{-1}. Hence, a has the same value in both experiments, while b has half its former value.

From the linear analysis of section 3 we obtain that the e-folding time for this case is 4.7 days compared to 7.1 days in the basic experiment. In the numerical simulation the growth is faster for the narrower jet, as expected. The general phenomenology, however, is similar in both experiments. The main differences between the two are: (i) The anticyclonic eddy $\mathbf{r}^1$ in the current experiment splits into two eddies—its southern part merges with $\mathbf{r}^2$ (Fig. 13c), while the northern part grows slowly into a strong eddy (Fig. 13d). (ii) The amplitude of the eddies $\mathbf{r}^4$ and $\mathbf{r}^5$ is about one-half of their previous value. (iii) Eddies $\mathbf{r}^4$ and $\mathbf{r}^5$ propagate here eastward along the coast, while in the basic experiment these eddies propagated toward the southeast. (iv) The radii of the anticyclonic eddies $\mathbf{r}^2$, $\mathbf{r}^4$, and $\mathbf{r}^5$ are about 24 km for the narrower jet, that is, 30%

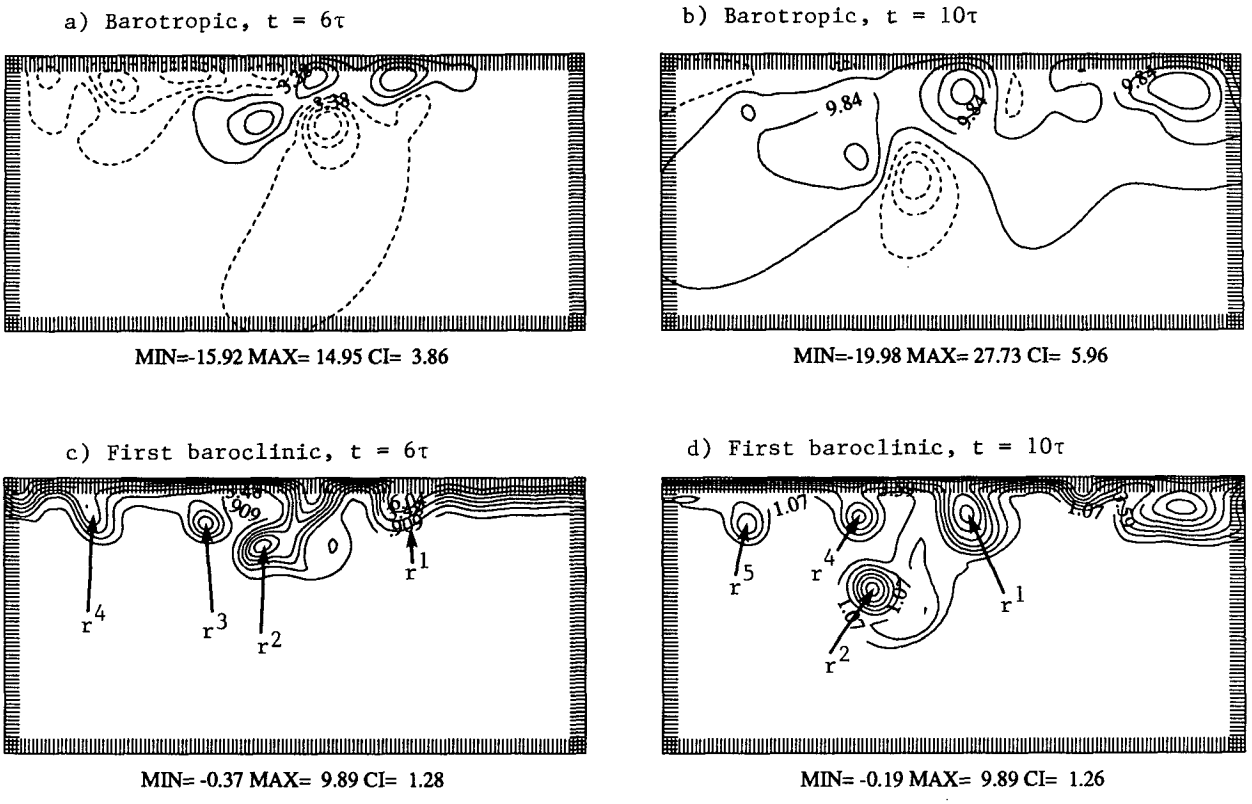

FIG. 13. The streamfunction for an experiment with a narrower downwelling zone along the coast: (a, b) the barotropic mode; (c, d) the first baroclinic mode; (a, c) $t = 6\tau$; (b, d) $t = 10\tau$. Same subdomain as in Figs. 3 and 11.

smaller than in the basic, broad-jet experiment. The latter phenomenon is intuitively obvious, while the former three are less so.

6. Concluding remarks

We have studied the instability of the westward current associated with downwelling along the south coast of Asia Minor. Both linear growth and subsequent eddy formation and detachment were studied using a quasi-geostrophic model with four vertical modes: one barotropic and three baroclinic ones (Fig. 1b).

Linear stability analysis of a basic state based on the results of Feliks (1991; see Table 1 and Fig. 1a here) showed that the most unstable wave has a length of about 100 km (Fig. 2a). This wavelength is remarkably independent of both the cross-shore scale of the downwelling front and the β effect (Table 2). The growth rate of this wave is proportional to the maximum speed of the coastal jet (Table 3), decreases as the horizontal jet's cross-shore scale decreases (Table 2), and is almost independent of the number of vertical modes (Table 2) and of the β effect (Table 3). The wave period is larger by an order of magnitude than the growth rate (Table 1), indicating linear growth of the instability nearly in situ, with little displacement.

The growth of the perturbation in the barotropic mode is due to cross-shore advection of the jet's potential vorticity by the perturbation of the first baroclinic mode. Conversely, the growth of the perturbation in the latter is mainly due to advection of the jet's potential vorticity, and hence streamlines, by the perturbation of the barotropic mode (section 3c, Figs. 3 and 4).

The subsequent evolution of eddies from the unstable jet, both weakly and fully nonlinear, was studied numerically with the same model. This evolution can be divided into three stages as follows.

1) The linear growth stage is dominated by numerical evolution of the perturbations in excellent agreement with the linear stability results. This stage lasts, for the standard parameter values of the basic experiment, about 16 days (twice the e-folding time).

2) The eddy-formation stage is when weakly nonlinear effects are the most important. A sharp increase in the amount of available potential energy transferred to kinetic energy occurs, and this transfer's contribution to the barotropic mode is dominant (Fig. 9). Consequently, several dipoles develop in this mode from the linear perturbation. Each ridge in the first baroclinic mode overlaps a barotropic dipole; the latter advects

the streamlines of the former, thus forming an isolated anticyclonic eddy. The radius of these baroclinic eddies is between 35 and 50 km.

3) During the nonlinear evolution stage, anticyclonic eddies—having detached themselves from the coastal jet—propagate toward the southwest or southeast. The propagation track of each isolated anticyclonic baroclinic eddy is determined mainly by the propagation of the barotropic dipole on which it rides, since the dipole advects the baroclinic eddy as it propagates. During this stage, the energy transfer between the different modes is much smaller than during the preceding one. The evolution of isolated eddies during this stage is very similar to the evolution of an isolated vortex investigated by Feliks (1990).

A sensitivity study of the dependence of the main results on several parameters shows the following. (i) The β effect has a significant role in the last, fully nonlinear stage of the evolution, accelerating the westward and southward propagation of the anticyclonic eddies. In the barotropic mode, exclusion of the β effect causes a dipole to rotate around itself. (ii) The evolution in models with two and four vertical modes is very similar, except that during the last stage the anticyclonic eddies and associated barotropic dipoles propagate more toward the east in the two-mode model. (iii) An increase of horizontal resolution to better resolve the higher baroclinic modes did not show significant differences in the formation and propagation of the barotropic dipoles or baroclinic monopoles. The only difference was that on the finer grid the eddies are less diffuse; this effect can also be obtained on the coarser grid by using higher-order numerical dissipation.

We also examined the effect of the horizontal, cross-shore scale of the downwelling front on the results. Assuming that the downwelling near the coast penetrates to the same depth independently of this scale, the maximum speed of the coastal current is inversely proportional to the horizontal scale. It was found that the stability of the front increases with the horizontal scale: when the scale is smaller, so is the radius of the eddies and, more often than not, their intensity.

These results are consistent with the idea that the warm- and salty-core eddies observed in the Eastern Mediterranean in recent years arise from the instability of the downwelling front along the northeastern coast of the Eastern Mediterranean (Feliks 1991). This idea is based on the similarity between the available observations and our analytical and numerical results. The radius of the eddies obtained in our basic simulation fits the radii of the observed eddies (35–50 km), and the thermal structure of the calculated and observed eddies is very similar. Furthermore, Ozsoy et al. (1989) observed along the Asia Minor coast a series of three eddies that masked the coastal current and persisted for the duration of their observations. In our simulations, a similar number of anticyclonic eddies form along the coast, with the downwelling jet's streamlines being detached from the coast and absorbed into the eddies, leading to a persistent, localized inhibition of westward velocity along the coast.

The present model was designed for a relatively straightforward process study. Given its simplicity, the similarity between model results and the existing, somewhat limited observations is rather striking. A more detailed simulation of the eddy phenomenology near the Anatolian coast would require first of all a much higher observational resolution, in space and time, of the flow and thermodynamic fields there. It would also require including coastline curvature in the model topography as well as thermodynamic forcing. We plan to do the latter in a primitive equation model based on Feliks (1991) while waiting for more detailed field data to compare with prospective simulation results.

A pervasive and robust combination of barotropic dipoles and baroclinic riders arises in the weakly nonlinear stage of the coastal-current instability growth and characterizes isolated-eddy propagation in the fully nonlinear phase. It is tempting to conjecture that this combination might play a role in the open ocean as well as, in particular, in the meandering and ring formation of western boundary currents. Such a role could help clarify the connection between the observed monopole aspect of baroclinic Gulf Stream (Parker 1971) and Kuroshio (Cheney and Richardson 1977) rings on the one hand and the remarkable stability of barotropic dipoles, numerical (McWilliams et al. 1991) and analytical (Sakuma and Ghil 1991), on the other.

Acknowledgments. YF is grateful to the staff of the Department of Atmospheric Sciences at UCLA and MG to that of the Laboratoire de Météorologie Dynamique du CNRS, Ecole Normale Supérieure, Paris, for their respective hospitalities during the sabbaticals spent at these institutions. It is a pleasure to thank B. Gola, K. Mah, and C. Wong for help with the typing, and K. Martelli for help with the figures. Comments from two anonymous reviewers have contributed to improve the presentation. This work was supported by a grant from the University of California's INCOR Global Change Modeling Project (YF), by ONR Grant N00014-89-J-1845 (YF and MG), and by a Guggenheim Fellowship (MG).

REFERENCES

Charney, J. G., 1971: Geostrophic turbulence. *J. Atmos. Sci.*, **28**, 1087–1095.

Cheney, R., and P. Richardson, 1977: Trajectory of a satellite-track buoy in a Kuroshio cold ring. *Polymode News*, **21**.

Feliks, Y., 1990: Isolated vortex evolution in 2 and 4 mode models. *Deep-Sea Res.*, **37**, 571–591.

——, 1991: Downwelling along the northeastern coasts of the Eastern Mediterranean. *J. Phys. Oceanogr.*, **21**, 511–526.

——, and S. Itzikowitz, 1987: Movement and geographical distribution of anticyclonic eddies in the Eastern Levantine Basin. *Deep-Sea Res.*, **34,** 1499–1508.

Flierl, G. R., 1978: Models of vertical structure and the calibration of two-layer models. *Dyn. Atmos. Oceans,* **2,** 341–381.

Fu, L. L., and G. R. Flierl, 1980: Nonlinear energy and enstrophy transfer in a realistically stratified ocean. *Dyn. Atmos. Oceans,* **4,** 219–246.

Ghil, M., and N. Paldor, 1991: Nonlinear wavelength selection and amplitude evolution for waves on a density front. *Phys. Fluids A,* in press.

Haidvogel, D. B., and W. R. Holland, 1978: The stability of ocean currents in eddy-resolving general circulation models. *J. Phys. Oceanogr.*, **8,** 393–413.

——, A. R. Robinson, and E. E. Schulman, 1980: The accuracy, efficiency and stability of three numerical models with application to open ocean problems. *J. Comput. Phys.*, **34,** 1–53.

Hecht, A., N. Pinardi, and A. R. Robinson, 1988: Currents, water masses, eddies and jets in the Mediterranean Levantine Basin. *J. Phys. Oceanogr.*, **18,** 1320–1353.

Hukuda, H., 1982: Subharmonic destabilization off Vancouver Island, *J. Phys. Oceanogr.*, **12,** 285–292.

Ikeda, M., 1983: Linear instability of current flowing along a bottom slope using a three-layer model. *J. Phys. Oceanogr.*, **13,** 208–223.

McWilliams, J. C., and G. R. Flierl, 1979: On the evolution of isolated, nonlinear vortices. *J. Phys. Oceanogr.*, **9,** 1155–1182.

——, ——, V. D. Larichev, and G. M. Rezhnik, 1981: Numerical studies of barotropic modons. *Dyn. Atmos. Oceans,* **5,** 219–239.

Mied, R. P., and G. J. Lindemann, 1982: The birth and evolution of eastward-propagating modons. *J. Phys. Oceanogr.*, **12,** 213–230.

Mysak, L. A., 1977: On the stability of the California undercurrent off Vancouver Island. *J. Phys. Oceanogr.*, **7,** 904–917.

Ozsoy, E., A. Hecht, and U. Unluota, 1989: Circulation and hydrography of the Levantine Basin: Results of POEM coordinating experiments 1985–1986. *Progress in Oceanography,* Vol. 22, Pergamon, 125–170.

Paldor, N., and M. Ghil, 1991: Shortwave instabilities of coastal currents. *Geophys. Astrophys. Fluid Dyn.*, **58,** 225–241.

Parker, C., 1971: Gulf Stream rings in the Sargasso sea. *Deep-Sea Res.*, **18,** 981–993.

Rhines, P. B., 1977: The dynamics of unsteady currents. *The Sea,* Vol. 6, E. D. Goldberg, I. N. McCane, J. J. O'Brien, and J. H. Steele, Eds., Wiley, 189–318.

Sakuma, H., and M. Ghil, 1991: Stability of propagating modons for small-amplitude perturbations. *Phys. Fluids A,* **3,** 408–414.

Salmon, R., 1978: Two-layer quasi-geostrophic turbulence in a simple case. *Geophys. Astrophys. Fluid Dyn.*, **10,** 25–52.

Shapiro, R., 1970: Smoothing, filtering, and boundary effects. *Rev. Geophys. Space Phys.*, **8,** 359–387.

Smith, B. T., J. M. Boyle, J. J. Dongarra, B. S. Garbow, Y. Ikebe, V. C. Klema, and C. B. Moler, 1976: *Matrix Eigensystem Routines—EISPACK Guide,* Springer-Verlag, 387 pp.